Chapter 3

3.1 Introduction

In this chapter, we have systematically studied the structural evolution of HfO_2 nanoparticles after doping with Dy concentration ranging from 1 to 11 at%. The monoclinic phase of HfO_2 transforms to the high temperature cubic phase when Dy concentration reaches 11 at%. The high temperature cubic phase remains stable at room temperature. The intermediate concentration of Dy shows a mixed phase of monoclinic and cubic. No such structural transformation from monoclinic to cubic by doping Dy in HfO_2 nanoparticles has been reported in the literature. Surprisingly, while the room temperature ferromagnetic behaviour observed in HfO_2 is quenched after doping of 1 at% of Dy, the photoluminescence studies show excellent emissions of blue and yellow light. A systematic study on structural, microstructural, magnetic and photoluminescence properties of Dy doped HfO_2 nanoparticles are discussed in this chapter.

3.2 Results and Discussion

3.2.1 Elemental Analysis

The composition of the pure and Dy doped HfO_2 samples have been examined using EPMA. In EPMA technique, the high energy electron beam is incident on a sample surface that generates X-rays of different wavelengths. These X-rays generated through atomic transitions between different shells are then captured by specific crystal monitor present in the instrument.[106, 107] Back scattered electron (BSE) imaging has been employed to investigate distribution of constituting elements having high and low atomic

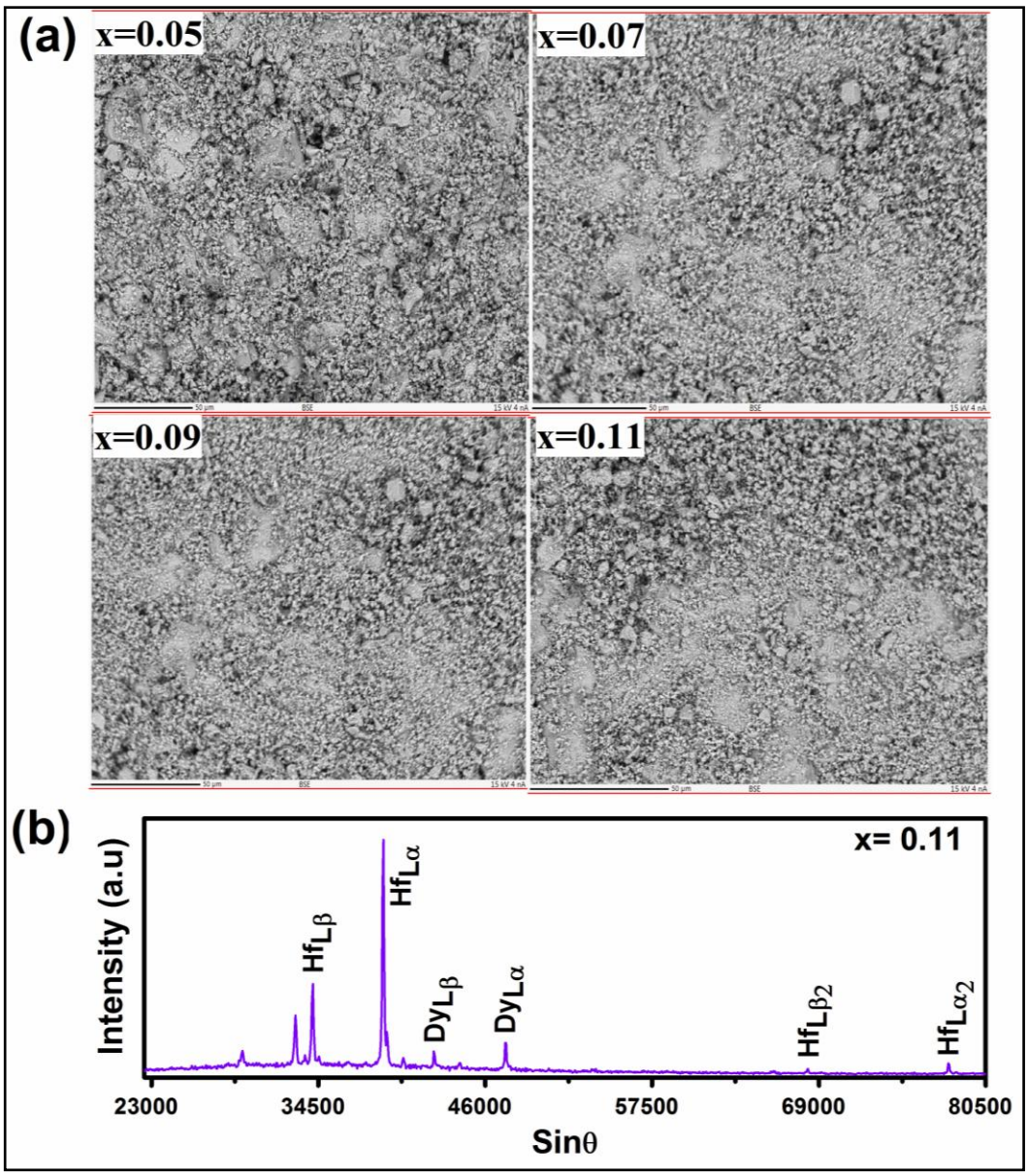

Figure 3.1 (a) *Back scattered electron (BSE) images for x = 0.05, 0.07, 0.09 and 0.11, respectively and* ***(b)*** *Wavelength dispersive spectra (WDS) for x = 0.11.*

numbers as depicted in **figure 3.1 (a)** for x = 0.05, 0.07, 0.09 and 0.11, respectively. The contrast of different areas obtained in BSE image is not similar everywhere since it is dependent of the atomic number of constituting elements. Thus, BSE images contain reliable information regarding portion of higher atomic number elements are brighter, areas

having low atomic number elements show lower contrast.[107] All BSE images explicitly show a uniform distribution of constituting elements present in Dy doped HfO_2. Wavelength dispersive spectra (WDS) have also been taken for prepared samples shown in **figure 3.1 (b)** for x = 0.11. WDS spectra confirm the presence of majority species i.e. Hf and a trace of Dy in Dy doped HfO_2. The dominant peaks corresponding to Hf can be clearly seen and have been indexed as $Hf_{L\alpha}$, $Hf_{L\alpha 2}$, $Hf_{L\beta}$, and $Hf_{L\beta 2}$, respectively. The peaks associated with Dy have been labeled as $Dy_{L\alpha}$ and $Dy_{L\beta}$.

3.2.2 Structural Analysis and Phase Transformation

X-ray diffraction (XRD) patterns of HfO_2 calcined at 500, 700 and 900 ^oC have been measured to examine the phase and crystallinity of the particles (**figure 3.2**). While

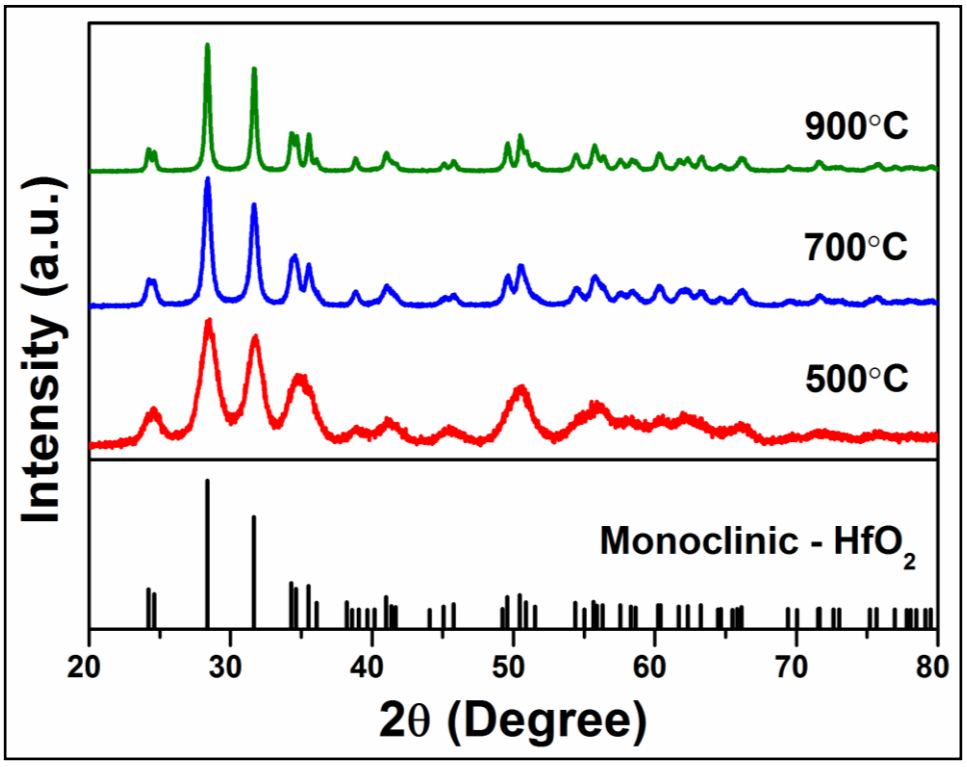

Figure 3.2 *X-ray diffraction patterns of HfO_2 calcined at 500, 700 and 900 ^oC.*

sample calcined at 500 ºC exhibits broad diffraction peaks indicating fine particles, with an increase in calcination temperature to 900 ^{o}C, diffraction peaks are well distinguished and become sharper indicating well crystalline nature . The observed diffraction peaks such as (011), (110), ($\bar{1}$11), (111), (020), (200), (021), ($\bar{2}$11) and (112) are well matched with the monoclinic phase (*m*-phase) of HfO_2 with space group, $P2_1/c$ (JCPDS card no. 78-0049). No impurity phase has been identified within the detection limit of the instrument. As the HfO_2 powders show well crystalline nature, we have fixed the calcination temperature at 900 ^{o}C for HfO_2 doped with the various concentration of dysprosium (Dy).

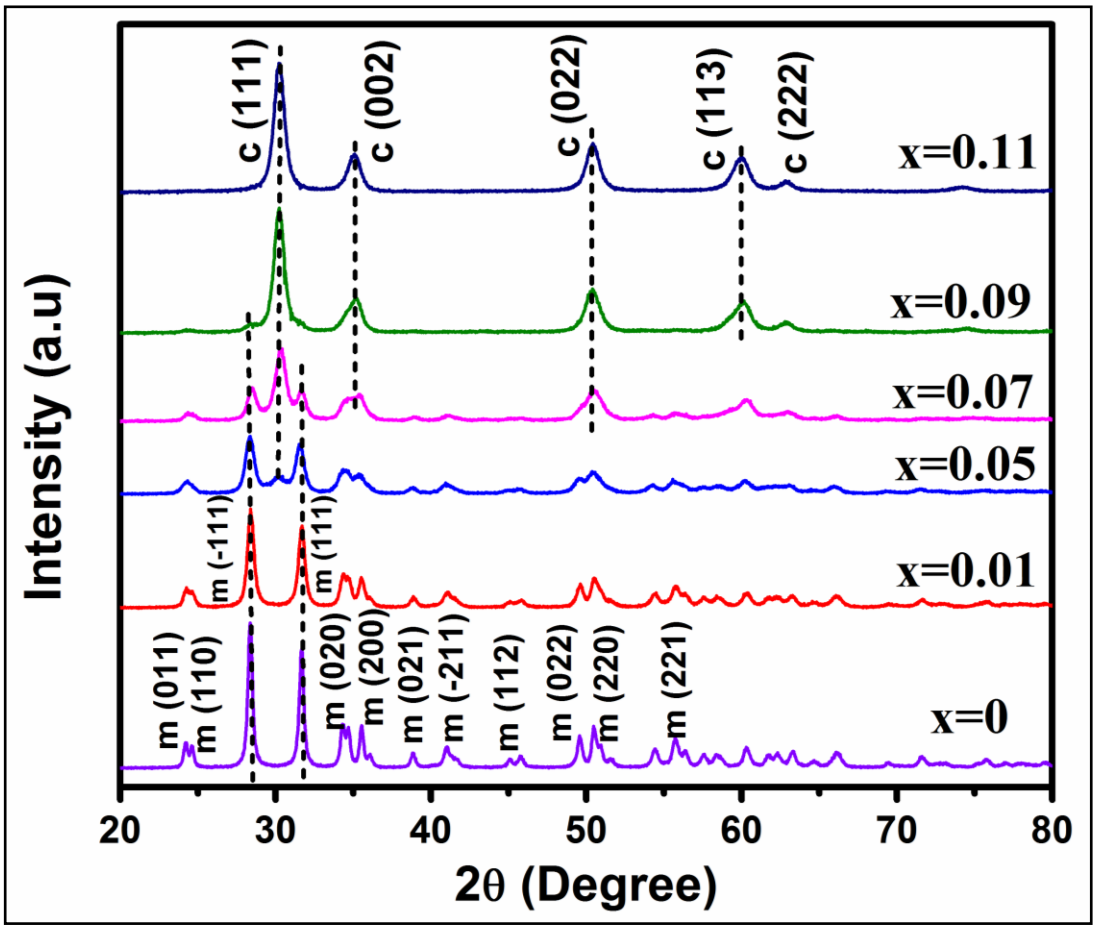

Figure 3.3 *XRD patterns of $Hf_{1-x}Dy_xO_2$ ($0 \leq x \leq 0.11$) samples calcined at 900 ^{o}C.*

XRD patterns of $Hf_{1-x}Dy_xO_2$ ($0 \leq x \leq 0.11$) are shown in **figure 3.3**. At lower Dy concentration (x = 0.01), the diffraction peaks are matched with the monoclinic phase as in pure HfO_2 except for the decrease in peak intensity. However, in x = 0.05, in addition to the peaks corresponding to the monoclinic phase, a weak characteristic peak at $2\theta = 30.20^o$ is observed, which matches with the (111) of cubic phase (JCPDS card no. 53-0560). At x = 0.07, diffraction peaks observed in XRD pattern correspond to the mixed phase of monoclinic and cubic. At x = 0.09, cubic phase becomes more pronounced at the expense of monoclinic one. At the highest dopant concentration i.e. x = 0.11, characteristic diffraction peaks along (111), (002), (022), (113) and (222) planes correspond to pure cubic phase (*c*-phase) of HfO_2 with space group, $Fm\bar{3}m$ (JCPDS card no. 53-0560). No peak of Dy_2O_3 phase is found in any Dy doped HfO_2 samples. This suggests that Dy^{3+} ions substitute Hf^{4+} ions in both monoclinic and cubic lattice. For the first time, we show that monoclinic phase of HfO_2 transforms to the high temperature cubic phase by doping Dy upto 11 at%. The high temperature cubic phase of HfO_2 becomes stable at room temperature.

Further, we have fitted the XRD patterns for x = 0 and 0.11 using Le-Bail profile fitting of FULLPROF program with pseudo-Voigt function, shown in **figure 3.4**. Pure HfO_2 is fitted with $P2_1/c$, monoclinic phase and x = 0.11 is fitted with $Fm\bar{3}m$ corresponding to the cubic phase. **Table 3.1** summarizes the extracted cell volume and cell parameters from Le-Bail refinement. It is worth to mention that incorporation of Dy in HfO_2 lattice increases the lattice parameter of the pure cubic phase of HfO_2 5.095 to 5.119 Å for x = 0.11. It may be vividly observed that while no significant change in cell volume of monoclinic phase is observed, cubic phase shows an increase of 1.4%. The observed

increase in cell volume of the cubic phase further confirms the replacement of Hf^{4+} ions with Dy^{3+} which is having relatively larger ionic radius than Hf^{4+} ion. This clearly indicates that a significant number of Dy^{3+} ions acquiring Hf^{4+} ion sites stabilize the high symmetry cubic phase even at room temperature. We have estimated the phase fraction by the integral peak area ratio of the cubic peak (111) to monoclinic peak (111) or ($\bar{1}$11).

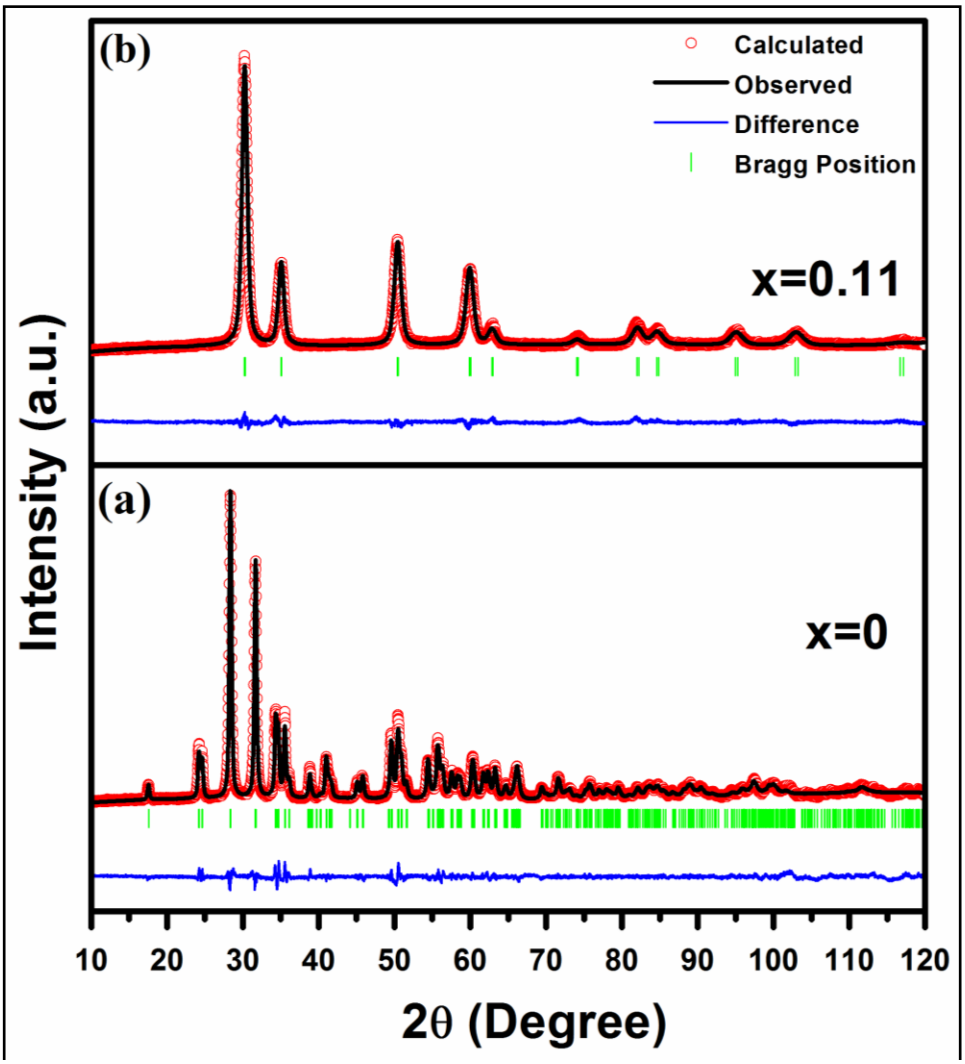

Figure 3.4 *Le-Bail profile fitting of XRD patterns using FULLPROF program* ***(a)*** *x = 0 with $P2_1/c$ and* ***(b)*** *x = 0.11 with $Fm\bar{3}m$.*

JCPDS card no./Sample	Space group	Cell parameters			
		a (Å)	b (Å)	c (Å)	Volume (Å^3)
78-0049	$P2_1/c$	5.117	5.175	5.291	138.32
53-0560	$Fm\bar{3}m$	5.095	5.095	5.095	132.26
$Hf_{1-x}Dy_xO_2$ (x = 0)	$P2_1/c$	5.117	5.176	5.290	138.302
$Hf_{1-x}Dy_xO_2$ (x= 0.11)	$Fm\bar{3}m$	5.119	5.119	5.119	134.12

Table 3.1 *Standard JCPDS data for monoclinic and cubic phase of HfO_2 and refined cell parameters for $Hf_{1-x}Dy_xO_2$ (x = 0 and 0.11).*

Variation of $A_{CP(111)}/A_{MP(111)}$ or $A_{MP(T11)}$ with Dy concentration reveals that peak integral area ratio increases with increasing Dy concentration. While both the monoclinic and cubic phases coexist at an intermediate Dy concentration (x = 0.05 - 0.09), a complete cubic phase is eventually observed when x = 0.11. Williamson-Hall (W-H) method is employed to separate the particle size and lattice strain of the XRD line broadening using the following equation (1).[108]

$$\frac{\beta \mathrm{Cos}\,\theta}{\lambda} = \frac{k}{D} + \frac{4\varepsilon \mathrm{Sin}\,\theta}{\lambda} \qquad (1)$$

where β is full width at half maximum (FWHM in radians), k is constant related to shape of particle θ is Bragg angle, ε is lattice strain, D is the crystallite size and λ is the wavelength of X-ray.

In general, a plot drawn between 4Sinθ and βCosθ (straight line expected) allows one to extract the particle size and lattice strain from its intercept and slope, respectively. All samples show non-zero slopes indicating strain in both monoclinic and cubic lattices. The variation in particle size and lattice strain with Dy concentration are plotted as shown

in **figure 3.5**. In pure monoclinic phase, while particle size is of ~40 nm, pure cubic phase shows particles of around 10 nm in size. Although particle size is reduced by four times, the strain is increased by twice in cubic phase showing a maximum at 9 at% of Dy. One may note that strain is found to be higher in the range of 5 to 9 at% when the mixed phase of monoclinic and cubic is observed.

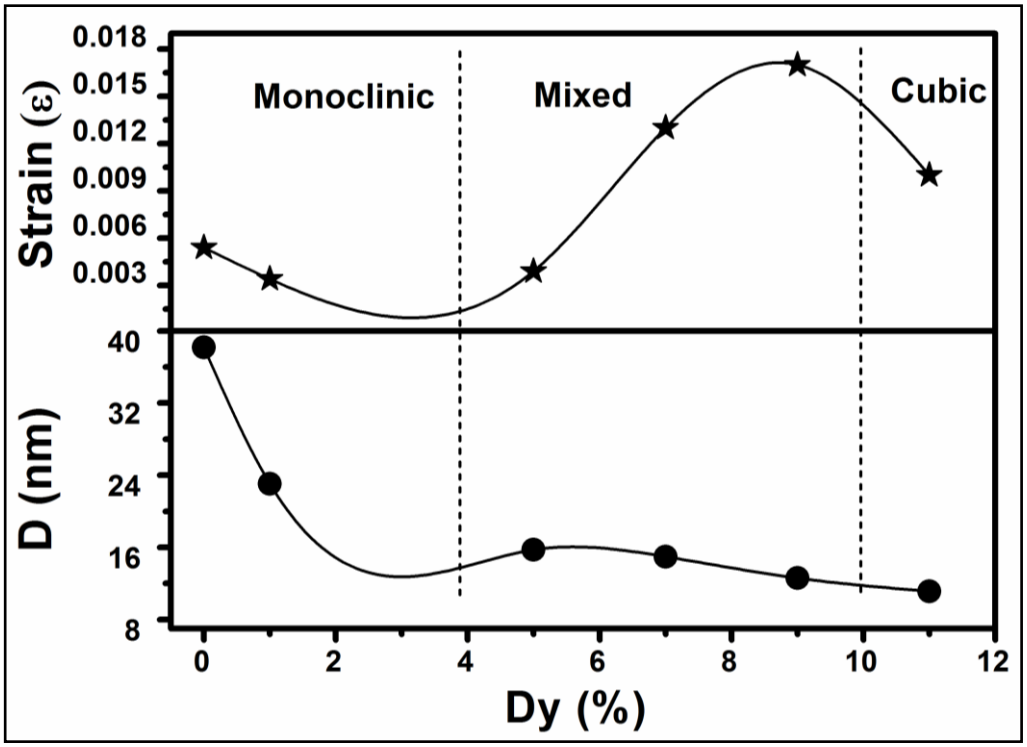

Figure 3.5 *Variation of crystallite size (D) and lattice strain (ε) in* $Hf_{1-x}Dy_xO_2$ *(*$0 \leq x \leq 0.11$*) samples.*

3.2.3 Microstructural Analysis

Transmission electron micrographs of monoclinic (x = 0) and cubic phase (x = 0.11) of HfO_2 show that the particles are slightly agglomerated and semi-spherical in shape (**figure 3.6**). From the particle size distribution histogram shown in the insets of **figure 3.7**

(a) and (c), the average particle size is found to be ~36 and ~10 nm for x = 0 and 0.11, respectively, which matches well with the estimated average particle size from W-H plot. **Figure 3.7 (a) and (c)** give the distinguished diffraction rings observed from the selected area electron diffraction (SAED) patterns indexed as ($\bar{1}$11), ($\bar{1}$02), ($\bar{1}$21) and ($\bar{2}$13) of $P2_1/c$ and (111), (200, (220) and (311) of $Fm\bar{3}m$. High resolution TEM shows the interplanar spacing (*d*) as ~0.28 and ~0.308 nm which corresponds to (200) and (111) of $P2_1/c$ and $Fm\bar{3}m$, respectively as depicted in **figure 3.7 (b) and (d)**.

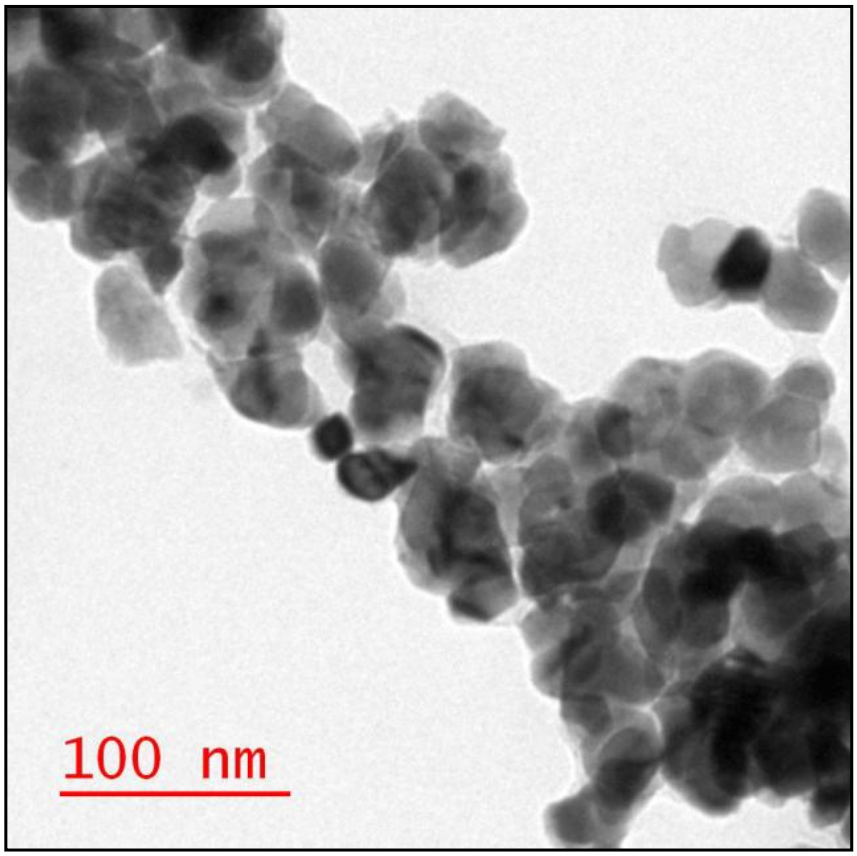

Figure 3.6 *Typical TEM micrograph of pure HfO_2 nanoparticles calcined at 900 ^oC.*

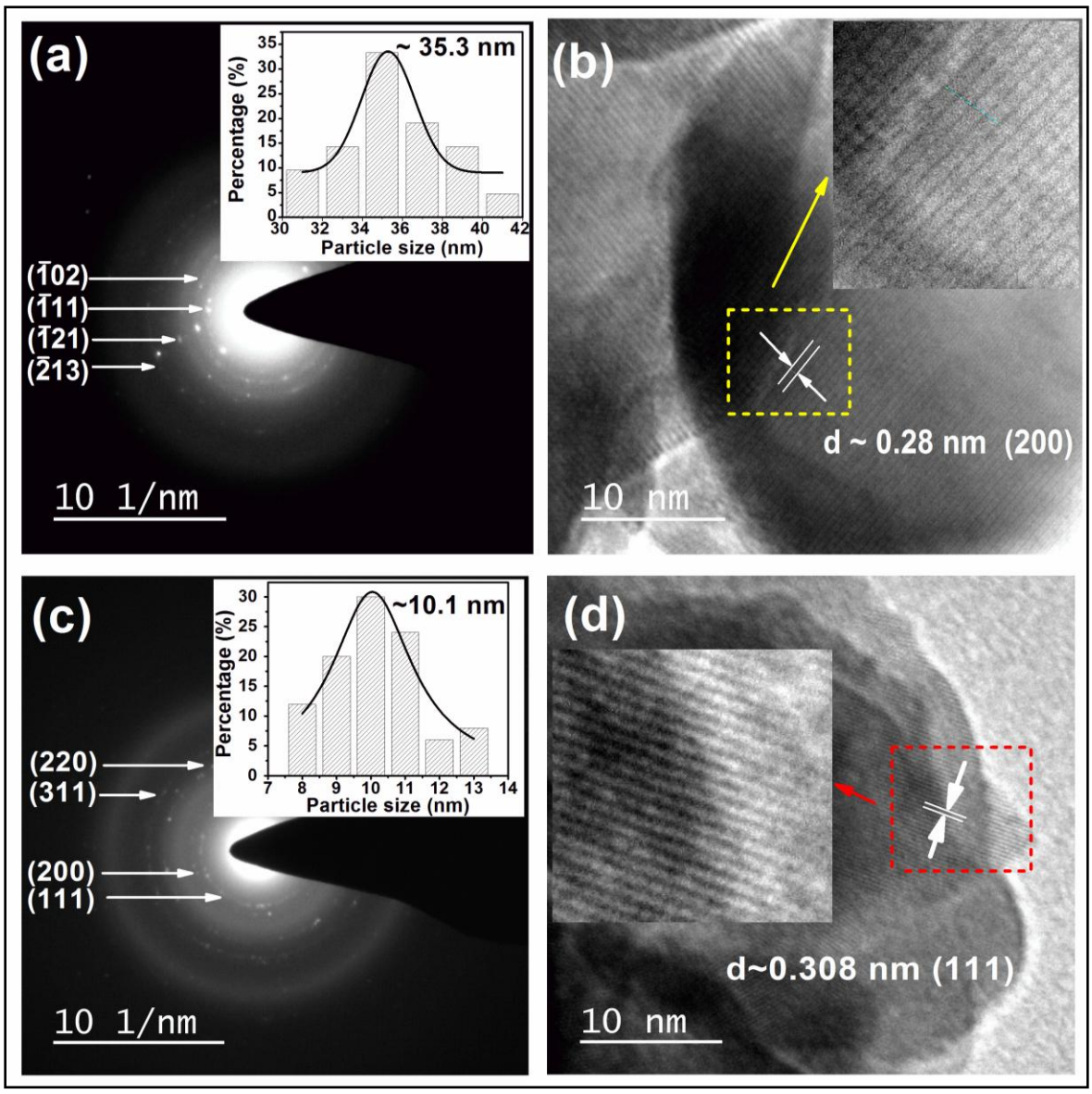

Figure 3.7 *SAED pattern and high resolution TEM for x = 0* ***(a and b)*** *and x = 0.11* ***(c and d),*** *respectively. Insets of* ***(a)*** *and* ***(c)*** *show the particle size distribution histogram. Insets of* ***(b)*** *and* ***(d)*** *show the lattice planes.*

3.2.4 Mechanism for Monoclinic to Cubic Phase Transformation

It is known in literature that bulk HfO_2 exists in polymorphs such as monoclinic phase at room temperature, tetragonal and cubic phases at around ~1700 and ~2600 ^{o}C, respectively. It has been reported earlier that the high temperature phases of HfO_2 can be

stabilized at room temperature effectively by various dopants like Mn, Ce, Lu and Y etc. of different chemical valancies.[54, 109-111] For example, Dohčević-Mitrović *et al*. demonstrate the complete stabilization of pure cubic phase in HfO_2 by doping 15% of trivalent yttrium by metathesis synthesis.[66] Gálvez-Barboza *et al.,* through simple modified sol-gel method, obtain the pure cubic phase of HfO_2 nanoparticles after doping with 10% of trivalent Ce.[55] Mendoza-Mendoza *et al.* also report successful stabilization of the cubic phase by doping 10 mol% of Ce at a lower temperature through a molten LiCl/KCl chloride flux method.[110] On the other hand, Gao *et al.* report a fully stabilized cubic phase after doping with multi-valent Mn in HfO_2 nanoparticles by conventional solid state reaction method.[109] It has been shown that doping with 30% of Mn in HfO_2 and sintering in an argon atmosphere, the transformation from Mn^{4+} to Mn^{2+} takes place that stabilizes the cubic phase. However, sintering at 1000 ^{o}C in the air, impurity phases of Mn_2O_3 and MnO are observed for more than 30% of Mn.[109] Furthermore, such high temperature cubic phase has not only been stabilized in HfO_2 but also in a similar system like ZrO_2. The key factors are the incorporation of dopants associated with the lattice expansion and consequent formation of oxygen vacancies. Therefore, the phase transformation from monoclinic to cubic in Dy doped HfO_2 could be explained in the light of stabilization process of doped ZrO_2 system.[112] It is a general agreement and is well accepted in literature that binary oxides are more prone to oxygen defects and to sample non-stoichiometry.[113, 114] Theoretically, Zhang *et al.*, through first principle calculation predicts that a divalent or trivalent cation substituting Hf^{4+} ion induces oxygen vacancies (V_o) in the host lattice to maintain the overall charge neutrality. These dopants lower the required formation energy to introduce an oxygen vacancy in the host lattice.[115] The low

temperature monoclinic phase possesses seven coordinated Hf^{4+} ions, whereas the high temperature tetragonal or cubic phase is coordinated by eight Hf^{4+} ions. Therefore, it is expected in the present case that addition of Dy^{3+} ions in HfO_2 lattice may also generate oxygen vacancies which vary with an increase in Dy concentration.

3.2.5 X-ray Photoelectron Spectroscopy (XPS)

XPS spectra for O 1*s* core level are shown in **figure 3.8** for x = 0 and 0.11. All the peaks are calibrated with respect to the C 1*s* peak located at ~284.6 eV. Due to the asymmetric shape of the spectra, we have deconvoluted the spectra into three peaks fitted with mixed Gaussian and Lorentzian functions using XPSPEAK version 4.1. The three curves centering at around 530.05, 531.1 and 533.0 eV are labeled as peak 1, 2 and 3, respectively. The peak with lower binding energy (BE) at 530.05 eV is associated with the oxygen atom in O—Hf^{4+} bond.[66] The higher BE peak at 531.1 eV belongs to O^{2-} ions in oxygen deficient regions in HfO_2 whereas peak at 533.0 eV originates partly from the hydroxyl groups and from the chemisorbed oxygen lying on the surface of the samples.[66, 116]

After deconvolution of each peak, due to the less pronounced peak corresponding to 533.0 eV in the spectra, we have ignored the area of the same peak. Comparing the peak area ratio of 2 and 1 (A_2/A_1), we observe that A_2/A_1 ratio is almost double in the cubic phase than in the monoclinic one. We, therefore, confirm that due to higher oxygen vacancies in x = 0.11, the high temperature cubic phase of HfO_2 is stabilized at room temperature. At the lowest concentration of Dy, HfO_2 shows only the monoclinic phase due to the insufficient amount of oxygen vacancy. With further increase in Dy concentration, the formation energy of oxygen vacancy is reduced significantly because of dipole formation between

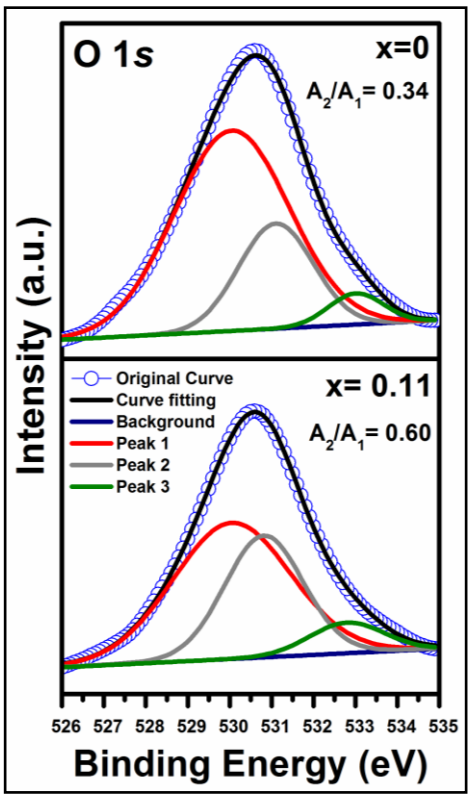

Figure 3.8 *The XPS spectra of O 1s region for x = 0 and x=0.11.*

Dy and V_o, introducing more oxygen vacancies in the lattice and hence, the monoclinic and cubic phases coexist for intermediate Dy concentrations (x = 0.05 - 0.07). Almost pure cubic phase is observed when Dy concentration approaches 9 at%. Eventually, at x = 0.11, a nominal concentration of oxygen vacancies is present that is sufficient enough to stabilize the cubic phase. Interestingly, one may notice that for dopants such as Y, Dy and Ce with ionic radii 1.019 Å, 1.027 Å and 1.143 Å, respectively i.e. more than Hf^{4+} and also more than 1.00 Å, need a lower concentration of dopants to stabilize the cubic phase at room temperature. On the other hand, a relatively much higher concentration of dopants is needed when the ionic radii of dopants like Mn^{2+} (0.96 Å) are slightly higher than Hf^{4+} but less than 1.00 Å. When the ionic radius (0.67 Å) of Mn^{4+} is quite less than the radius of Hf^{4+}, no cubic phase is observed even increasing the sintering temperature up to 1400 ^{o}C in

the air.[109] Further, it is known that the oxygen vacancies are present in different charge states such as V_o^{0}, V_o^{+} and V_o^{++} etc. Due to filled defects states, V_o^{0} does not essentially change the coordination number of Hf atoms and hence the relative phase stability. On the other hand, V_o^{++} is more efficient in reducing the relative energies of cubic phase of HfO_2 with respect to the monoclinic one. Therefore, after incorporating a sufficient amount of Dy in HfO_2, the charged oxygen vacancies associated to 7-fold coordinated Hf^{4+} ions around the defect site eventually result into 8-fold oxygen coordination with Dy^{3+} ion thereby stabilizing the cubic phase of HfO_2 at room temperature. The above observations clearly indicate that the enhancement in lattice volume and nominal oxygen vacancies are needed to stabilize the cubic phase at room temperature with low dopant concentration.

3.2.6 Magnetic Properties

The magnetization (*M*) as a function of magnetic field (*H*) at 300 K for pure HfO_2 (x = 0) calcined at 500, 700 and 900 ^{o}C are measured (**figure 3.9**). Sample calcined at 500 ^{o}C exhibits a slim hysteresis loop at the lower magnetic field and at higher field, a linear increase in magnetization is observed. With increasing calcination temperature to 900 ^{o}C, besides a linear increase in magnetization, the area under the hysteresis loop increases. The presence of noticeable hysteresis loop with low coercivity and remanence demonstrates a weak ferromagnetic behavior at room temperature induced primarily due to lattice defects. While coercivity (H_c) of ~45 Oe remains same in the sample calcined at 700 and 900 ^{o}C, the remanence (M_r) is enhanced by an order of magnitude in sample calcined at 900 ^{o}C. The observed H_c is comparable to H_c in HfO_2 reported by Coey *et al*.[117] In addition, it is worth noting that the maximum magnetization (M_{max}) decreases in sequence with

increasing calcination temperature. The reduction in M_{max} is attributed to decrease in the surface to volume ratio.

Due to an appreciable hysteresis loop observed in sample calcined at 900 ^{o}C, we have measured M vs. H at 2 and 35 K shown in **figure 3.10**. It is evident that the area under the hysteresis loop dramatically increases with decrease in measurement temperature as expected. At 2 K, while H_c is ~650 Oe, at room temperature, it drastically falls to ~45 Oe

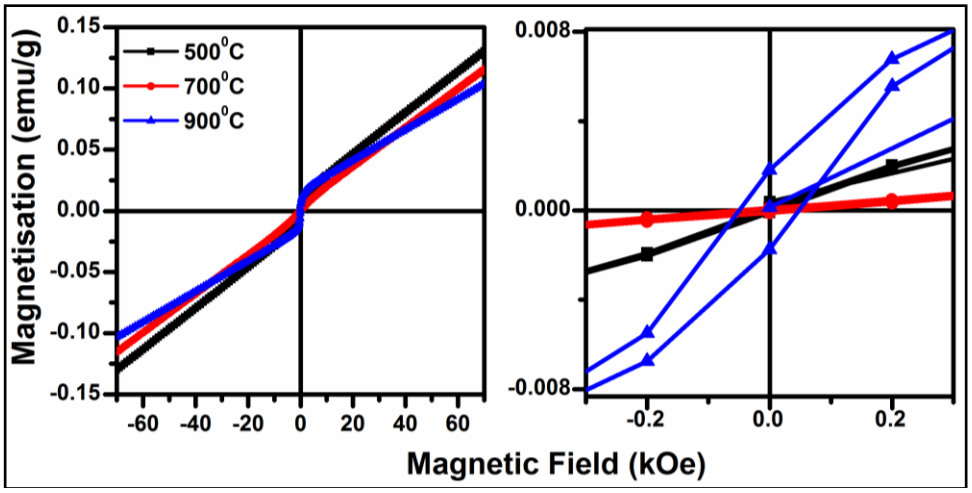

Figure 3.9 *Room temperature M vs.H curves for pure HfO_2 calcined at 500, 700 and 900 ^{o}C. The right panel shows hysteresis at low magnetic field.*

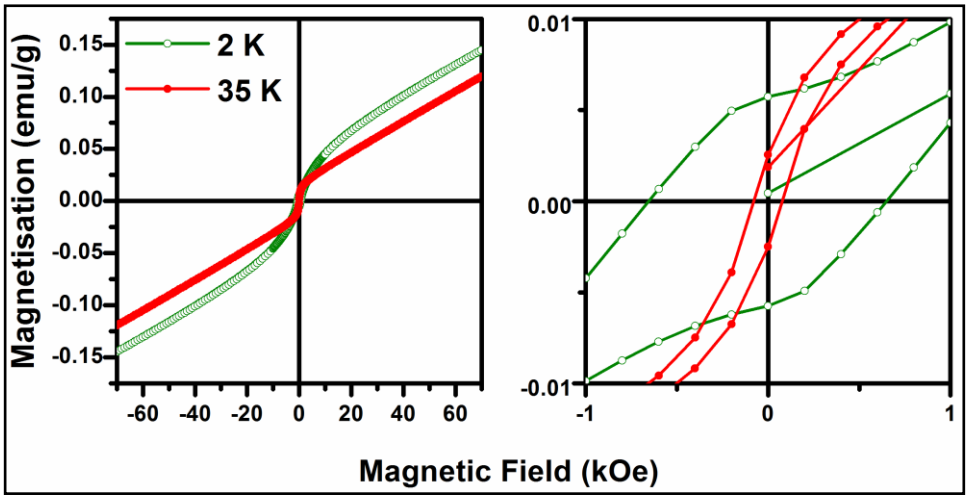

Figure 3.10 *M vs. H curves at 2 and 35 K for pure HfO_2 calcined at 900 ^{o}C.*

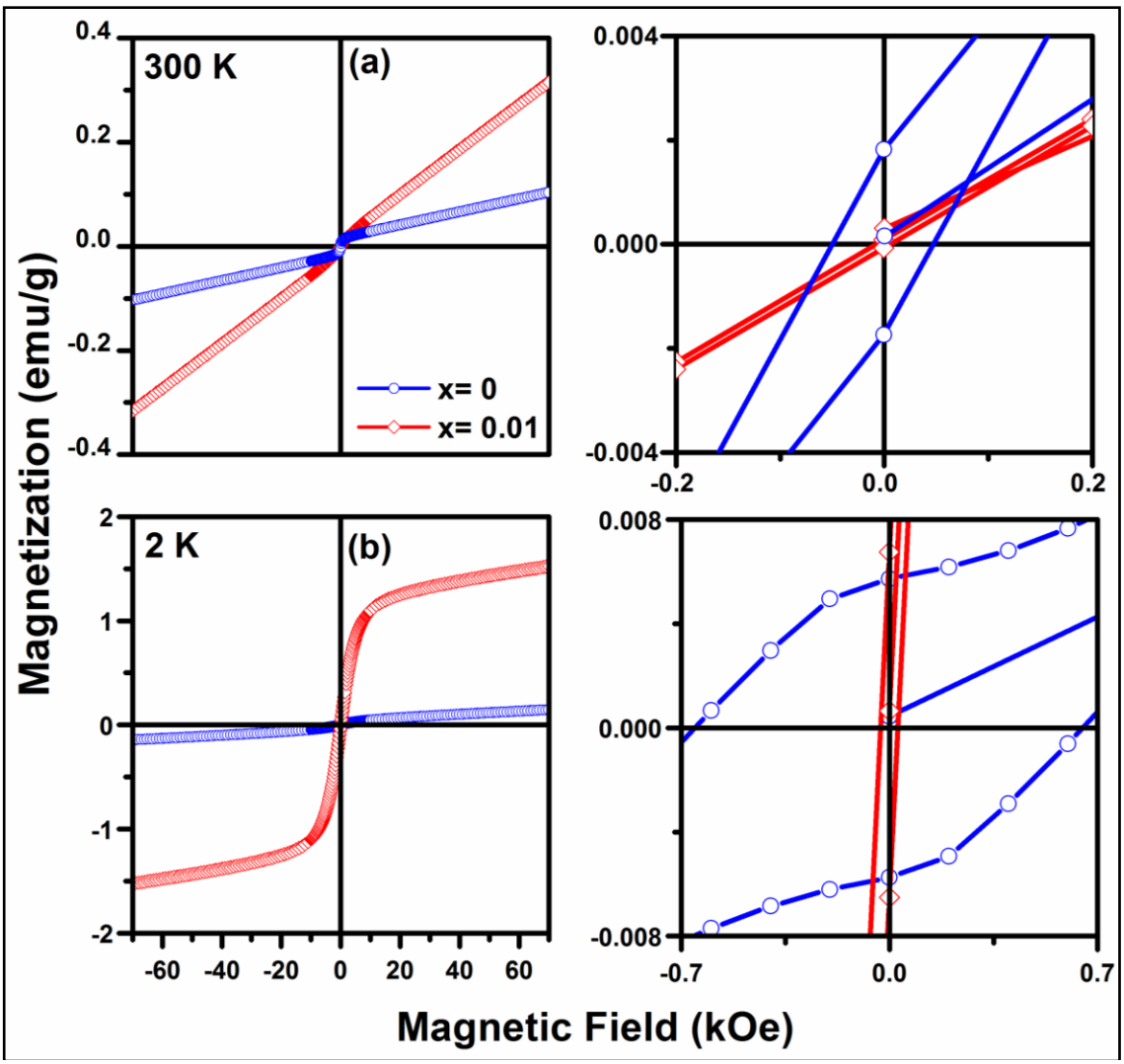

Figure 3.11 *M vs. H dependence measured at* ***(a)*** *300 K and* ***(b)*** *2 K for* $Hf_{1-x}Dy_xO_2$ *(x= 0 and 0.01). The right panel shows a zoomed-in view at lower field for x = 0 and 0.01.*

which is an order magnitude less. This indicates that ferro or ferrimagnetic ordering exist even at room temperature, which becomes more prominent at low temperature. Such a behavior is consistent with earlier reports on the colloidal HfO_2 nanorods, CaO nanopowders and CeO_2 powders.[118-120] While M_{max} enhances by 30% at 2 K, M_r increases from ~0.002 to ~0.006 emu/g with decreasing temperature from 300 to 2 K.

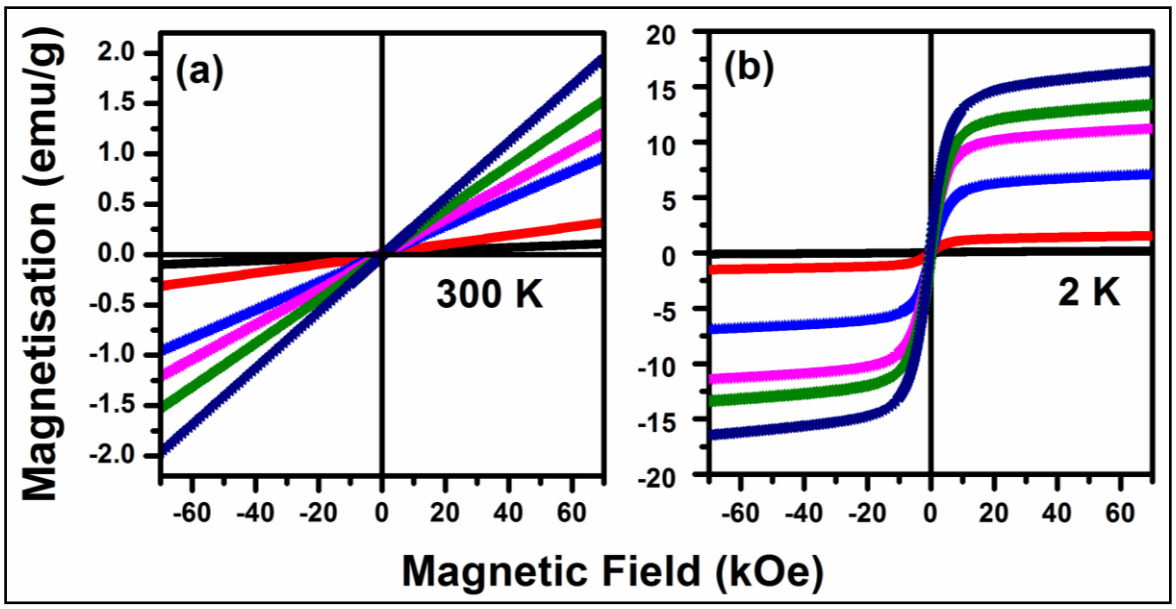

Figure 3.12 *M vs. H dependence measured at* ***(a)*** *300 K and* ***(b)*** *2 K for* $Hf_{1-x}Dy_xO_2$ *(x= 0-0.11).*

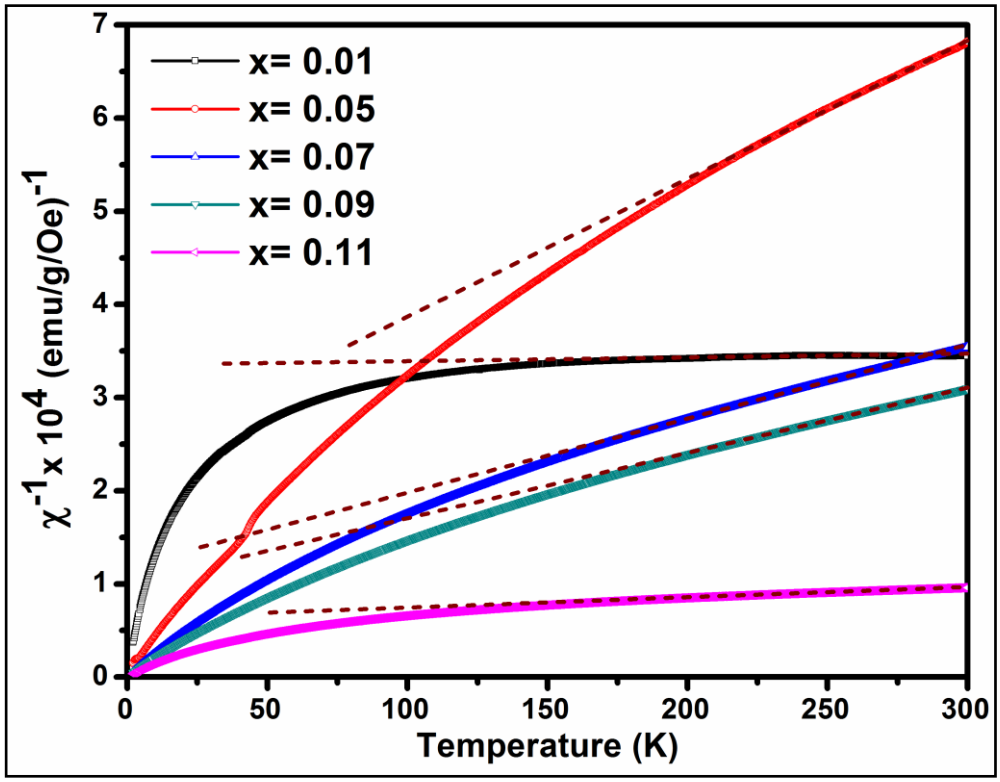

Figure 3.13 *Variation of* χ^{-1} *vs. T for* $Hf_{1-x}Dy_xO_2$ $(0.01 \leq x \leq 0.11)$.

Varying Dy concentration from 0 to 1 at% in HfO_2, we have shown M vs. H at room temperature in **figure 3.11 (a)**. Magnetization linearly increases with increasing magnetic field indicating paramagnetic behavior irrespective of Dy concentration. A closer inspection at low magnetic field reveals that addition of even 1 at% of Dy leads to a collapse of the hysteresis loop. This indicates severe quenching of the weak ferro or ferrimagnetic ordering observed in pure HfO_2 by doping Dy. However, M_{max} shows a proportional enhancement with increasing Dy concentration in HfO_2. On the other hand, at 2 K we observe well-saturated hysteresis loop for $Hf_{1-x}Dy_xO_2$ (x = 0 and 0.1) (**figure 3.11 (b)**). It is interesting to note that H_c drastically reduces from ~650 to ~30 Oe by incorporating 1 at% of Dy and remains unchanged for above concentration of Dy. An almost constant H_c value of ~25±5 Oe is observed for all samples having more than 1 at% of Dy concentration. Saturation magnetization (M_s) increases from 0.14 to 16.2 emu/g with increasing Dy concentration upto 11 at% (**figure 3.12**).

In order to confirm the ferro or ferrimagnetic nature in Dy doped HfO_2, we have extrapolated the high temperature regime in the Curie-Weiss plot which gives negative Curie-Weiss temperature depicted in **figure 3.13**. It suggests an antiferromagnetic (AFM) correlation at the low temperature. However, the presence of hysteresis loop at low temperature reflects the finite magnetic moment. Combining both experimental observations, we conclude that the non-compensated antiferromagnetically ordered spins results in a finite magnetic moment exhibiting a ferrimagnetic behavior at low temperature. Further, susceptibility measurements with varying temperature shown in **figure 3.14**, shows the transition from antiferro and/or ferrimagnetic to paramagnetic phase for x = 0,

0.05, 0.07 and 0.11. We show that while Néel temperature (T_N) for x = 0 is found to be 45.5 K, for x = 0.05, 0.07 and 0.11, T_N decreases to 4.6, 2.8 and 2.5 K, respectively.

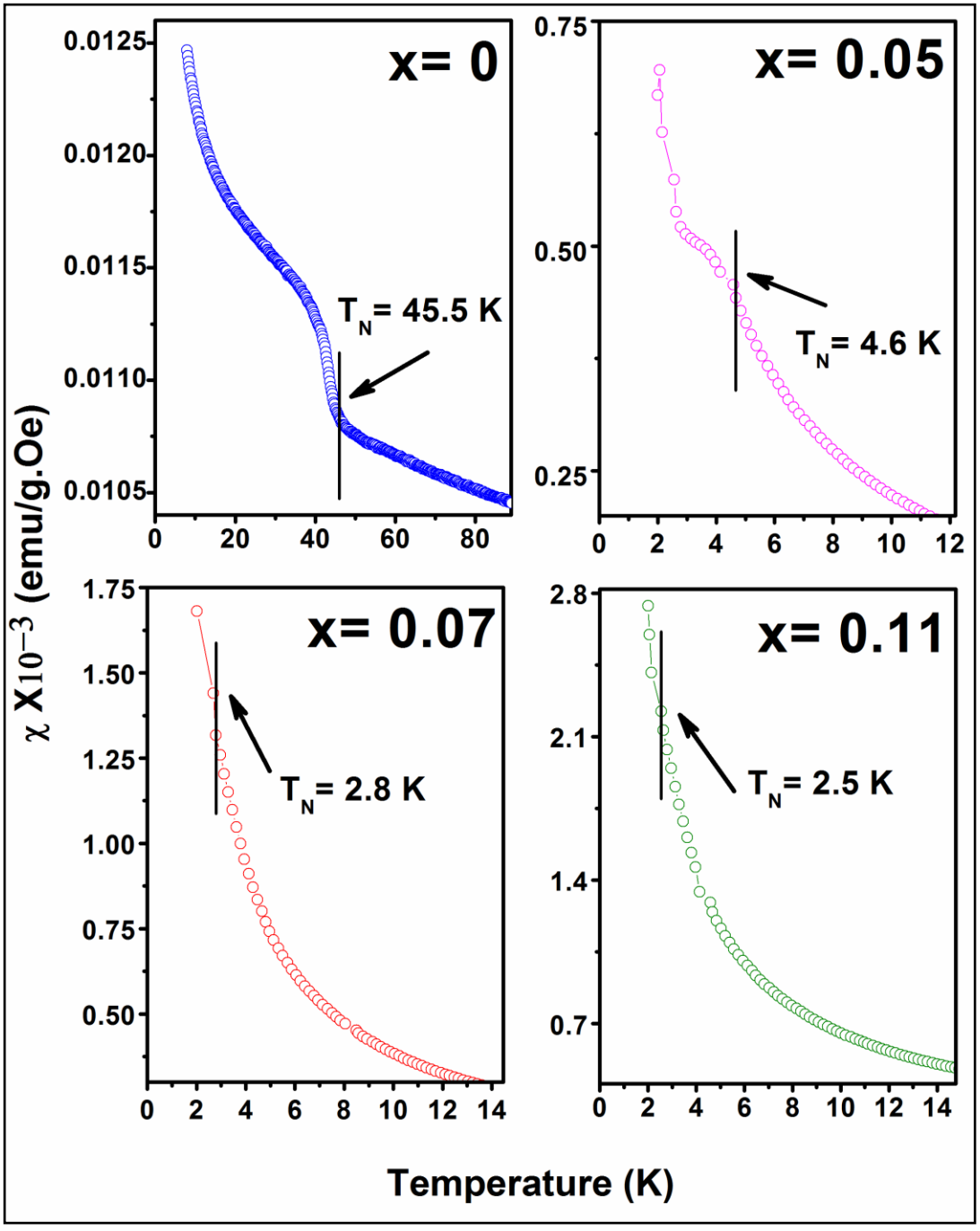

Figure 3.14 *Variation of susceptibility with temperature in $Hf_{1-x}Dy_xO_2$ (x = 0, 0.05, 0.07 and 0.11) nanoparticles.*

3.2.7 Origin of Room Temperature Ferromagnetism

It has been shown that RTFM in non-magnetic oxides like TiO_2, HfO_2, ZnO, SnO_2, Al_2O_3, MgO and CeO_2 is an inherent characteristic property of the nanostructured materials. The origin of such ferromagnetic ordering is likely due to various defects such as oxygen vacancies, F-centers, defect complexes etc and also depends on crystallinity, shape and morphology of the particles.[61, 77, 117, 119, 121-131] On the contrary to above reports, Lin *et al*. report the absence of ferromagnetic ordering in HfO_2 nanoclusters.[75] In this context, Dohčević-Mitrović *et al.* show that degradation of ferromagnetic ordering in Y doped HfO_2 could be due to various $(V_0{-}Y_{Hf})$ defect complexes in different charge states such as $(V_0{-}Y_{Hf})^0$, $(V_0{-}Y_{Hf})^+$ and $(V_0{-}Y_{Hf})^{++}$. Among them, $(V_0{-}Y_{Hf})^+$ is the most stable. Since these defects are usually located very near to the valence band, electrons could not be moved to 5*d* states to form the spin-split defect band to establish ferromagnetism.[66] On the other hand, in Pr doped CeO_2 nanoparticles, Paunović *et al.* believe that formation of $Pr^{3+}{-}V_0{-}Pr^{3+}$ or $Pr^{3+}{-}V_0{-}Ce^{3+}$ defect complexes are responsible for suppression of ferromagnetic ordering.[132] According to predictions using theoretical molecular mechanics method, generated oxygen vacancies mainly lie at the surface of nanoparticles that requires less energy to form an empty space corresponding to anions.[70] Also, oxygen vacancy at the surface is more efficient for mediating ferromagnetism than in the bulk.[131] These oxygen vacancies can exist in different charge states by electron trapping such as V_0^{--}, V_0^{-}, V_0, V_0^{+} and V_0^{++} forming defect band near the conduction band. It is well known that two electrons trapped in an oxygen vacancy called as F^0 centers are able to develop antiferromagnetic ordering while singly occupied vacancies (F^+ centers) establishes long range ferromagnetic ordering that lies deep in the impurity band gap. Also,

oxygen vacancies that are unoccupied known as F^{++} centers do not contribute to ferromagnetic ordering.[72, 73]

In the present case, XPS analysis revealed that pure HfO_2 exhibiting monoclinic structure contains a considerable amount of oxygen vacancies at the surface of nanoparticles. We believe that these induced oxygen vacancies mediate ferromagnetic ordering via F^{+} center exchange mechanism. The addition of Dy^{3+} ion produces an oxygen vacancy (V_0) may bring two electrons in lattice to compensate charge neutrality which increases with increase in Dy^{3+} concentration. In spite of a sufficient number of V_0, it is surprising that very small amount of substituted Dy^{3+} ions destroy the weak ferromagnetism observed in pure HfO_2. In view of above reports and considering our experimental facts, it appears that quenching of ferromagnetic ordering in Dy doped HfO_2 could be either due to partial compensation of F^{+} by F^{0} and/or F^{++} centers or because of defect states located far from the oxide conduction band minimum (CBM). However, it is obvious that substituted Dy^{3+} ions for Hf^{4+} ions in the lattice which are near to oxygen vacancy can create different kinds of unwanted complexes. In Dy doped HfO_2, a similar defect state of Dy^{3+}─V_0─Dy^{3+} type can also be possibly formed which basically creates oxygen vacancies with no trapped electrons (F^{++} centers). The abundant formation of F^{++} centers negates long range ferromagnetic ordering and partially reduces the number of F^{+} centers that hinders the appearance of ferromagnetism. On the other hand, defect complex formation can also displace the single electron energy levels of V_0 near or far from valence band maximum that prevents spin-splitting of defect bands developing ferromagnetism.[66, 133] Therefore, presence of Dy^{3+} ions in the HfO_2 lattice can cause a reverse effect leading to the manifestation of the ferromagnetic ordering in Dy doped HfO_2 system.

3.2.8 Photoluminescence Properties

Figure 3.15 depicts the room temperature excitation spectra recorded under emission wavelength of 490 nm for pure and Dy doped HfO_2 nanoparticles. In sample x = 0, the spectrum consists of a broad band in the range of 240 to 340 nm centered at ~296 nm and an another peak centered at ~398 nm. The former peak is attributed to the host absorption band.[54] The latter could originate from the most common defect state such as oxygen vacancies inherent in HfO_2. In x = 0.01, along with a host absorption peak at ~296 nm, the most intense peak is observed at 352 nm resulting from the electronic transition from the ground state, $^6H_{15/2}$ to hypersensitive, $^6P_{7/2}$. In addition, sharper secondary peaks are observed in the range of 300-410 nm. These peaks detected at around 326, 338, 366, 383 and 393 nm are ascribed to different f-f transitions of Dy^{3+} ions from the ground state, such as $^6H_{15/2} \rightarrow {}^6P_{3/2}$, $^6H_{15/2} \rightarrow {}^4F_{5/2}/{}^4I_{9/2}$, $^6H_{15/2} \rightarrow {}^6P_{5/2}$,$^6H_{15/2} \rightarrow {}^4F_{7/2}$, and $^6H_{15/2} \rightarrow {}^4I_{13/2}$, respectively.[134, 135] The presence of host absorption peak at ~296 nm indicates a weak energy transfer from the host to Dy^{3+} activator ions. Further, the intensity of these excitation peaks decreases with increasing Dy concentration and finally reaches a minimum when x = 0.11. The appearance of sharp absorption peaks after doping 1 at% of Dy occurs at the expense of host absorption band of HfO_2 lattice.

The emission spectra of $Hf_{1-x}Dy_xO_2$ ($0 \leq x \leq 0.11$) nanoparticles are collected after exciting with 352 nm which is the highest intensity excitation peak shown in **figure 3.16**. In x = 0, two emission peaks at 413 and 435 nm are superimposed and show a broad band in the range of 380-500 nm. These peaks are ascribed to the emissions of the host lattice. In addition to these peaks, for x = 0.01, two more emission peaks are observed at 490 and 577 nm falling in the blue and yellow region, respectively.

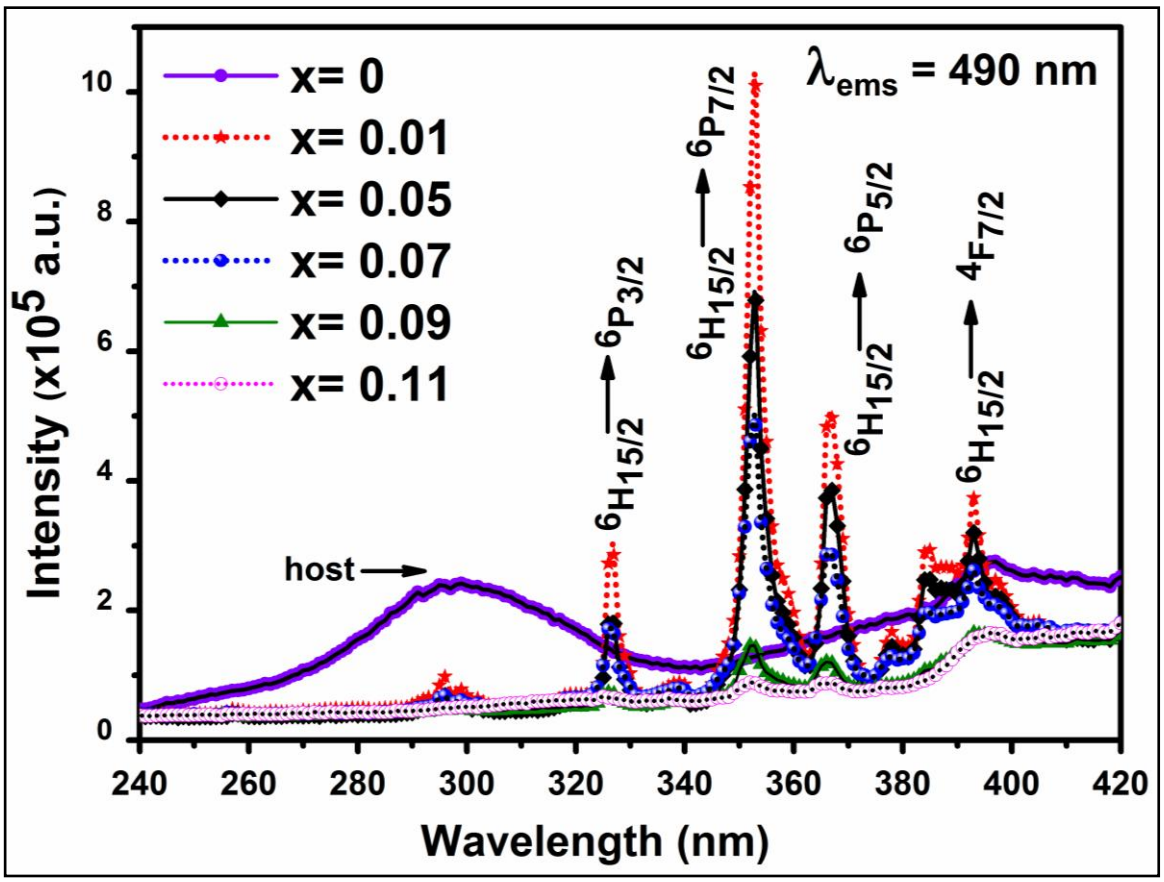

Figure 3.15 *Room temperature excitation spectra of* $Hf_{1-x}Dy_xO_2 (0 \leq x \leq 0.11)$ *by monitoring the emission wavelength at 490 nm.*

These peaks are the consequence of transitions from the metastable state to ground states such as $^4F_{9/2} \rightarrow {}^6H_{15/2}$ and $^4F_{9/2} \rightarrow {}^6H_{13/2}$.[135, 136] With increasing Dy concentration, the emission peak intensity decreases gradually up to 7 at% and further at x = 0.09 and 0.11, the peak intensity is drastically reduced. Moreover, we observe the most efficient emission behavior when we dope only 1 at% of Dy in HfO_2.

It is well-known that emission from the electronic transition, $^4F_{9/2} \rightarrow {}^6H_{13/2}$ of the Dy^{3+} ion observed in yellow (Y) region is hypersensitive to the crystal field environment. In a site without inversion symmetry, usually, this transition becomes the dominant one.[137] The other strongest emission peak corresponding to the magnetic transition, $^4F_{9/2}$

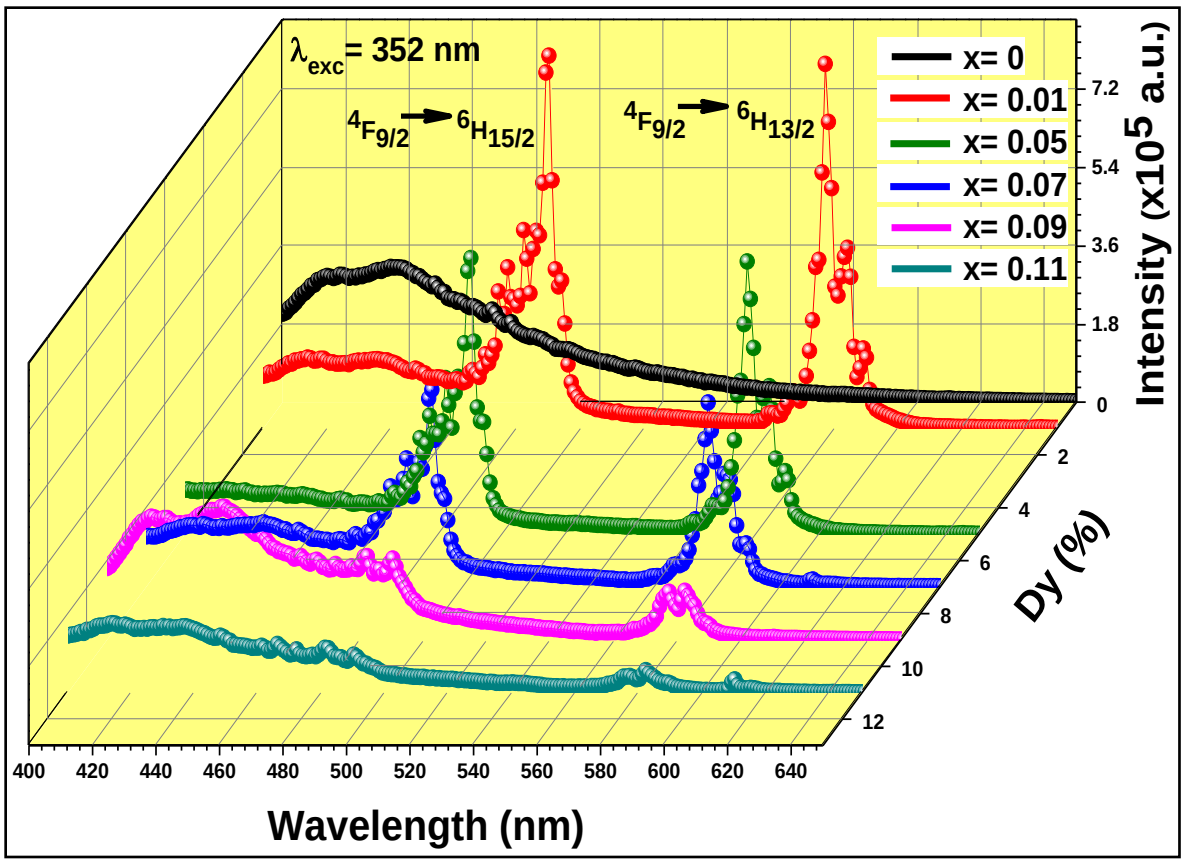

Figure 3.16 *Room temperature emission spectra of $Hf_{1-x}Dy_xO_2$ ($0 \leq x \leq 0.11$) at an excitation wavelength of 352 nm.*

$\rightarrow {}^6H_{15/2}$ detected in blue (B) region bears the information of the presence of Dy^{3+} ions at a low symmetry site with inversion symmetry. Taking the intensity ratio of electronic to magnetic transition shown in equation (2) gives the indication of the local symmetry of Dy^{3+} ion site.

$$\frac{Yellow\ (Y)}{Blue\ (B)} = \frac{I({}^4F_{9/2} \rightarrow {}^6H_{13/2})}{I({}^4F_{9/2} \rightarrow {}^6H_{15/2})} \qquad (2)$$

The estimated Y-B ratio decreases with increasing Dy concentration as shown in **figure 3.17 (a)** (blue line). One can notice that Y-B ratio found to be 0.95±0.03 at a lower Dy concentration and remains constant upto x = 0.07. However, at a higher Dy concentration,

i.e. at x = 0.09 and 0.11, the Y-B ratio reduces more rapidly, suggesting that the intensity of electronic transition decreases faster than that of the magnetic one.[73] The reduction in Y-B ratio above 7 at% of Dy concentration could be due to the changes in the local symmetry of Dy^{3+} ions in HfO_2 lattice. It is evident from XRD analysis that while a high symmetry cubic phase obtained in x = 0.09 and 0.11, at x = 0.01-0.07, the low symmetry monoclinic phase remains present in the parent HfO_2 lattice.

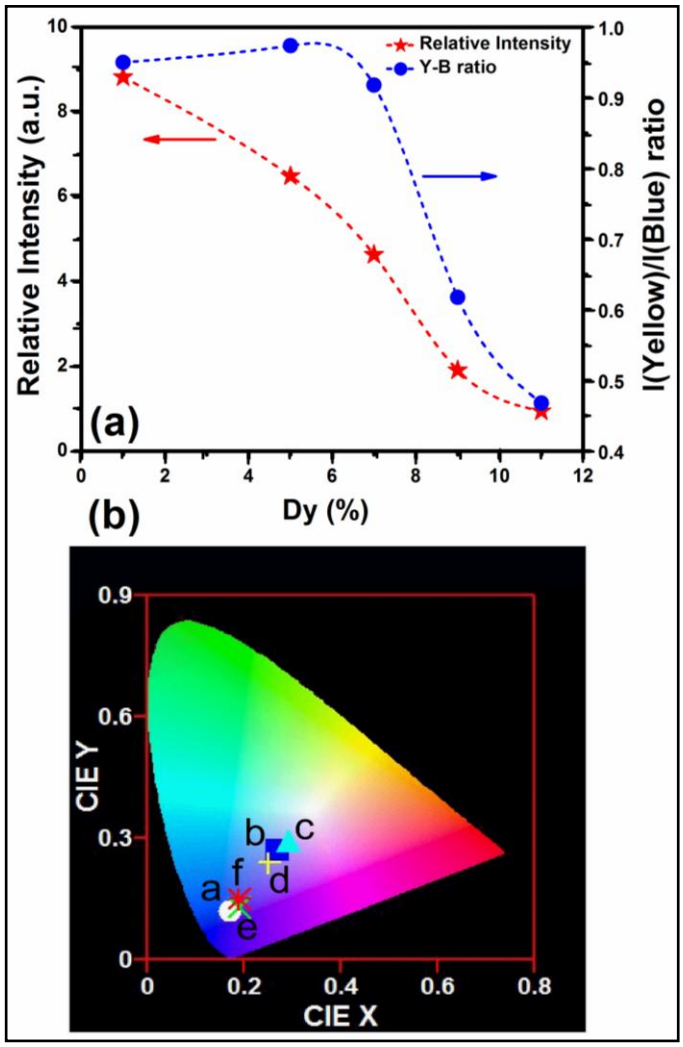

Figure 3.17 (a) *Dependence of Y–B ratio and the relative intensity of the 490 nm emission peak in* $Hf_{1-x}Dy_xO_2$ *(*$0 \leq x \leq 0.11$*) and* ***(b)*** *the CIE colour space chromaticity diagram (****a–f*** *corresponds to x = 0-0.11) under an excitation wavelength of 352 nm.*

The low symmetry in x = 0.01 and a high symmetry in x = 0.11 realized from XRD well supports the luminescence behavior as observed in the present case. **Figure 3.17 (a)** (red line) depicts the variation of relative intensity of emission peak at 490 nm as a function of Dy concentration in HfO_2 nanoparticles. The emission intensity decreases rapidly with increasing Dy concentration in HfO_2. Such a behavior clearly indicates the quenching of luminescence taking place due to increase in Dy concentration. At a higher Dy concentration, this can be best explained in terms of the cross relaxation between two closely situated Dy^{3+}–Dy^{3+} ions that includes mainly transition Dy^{3+} ($^4F_{9/2}$) + Dy^{3+} ($^6H_{15/2}$) → Dy^{3+} ($^6F_{3/2}$) + Dy^{3+} ($^6H_{11/2}$). Due to less separation between Dy^{3+} ions, the electrons move from a high energy level, $^4F_{9/2}$ to $^6F_{3/2}$ a lower energy level.[136-138] The energy associated with such transition helps electrons sitting in the ground state of Dy^{3+} activator ions to get transferred to a higher energy level, $^6H_{11/2}$. Such observation suggests that excellent photoluminescence properties can be perceived by doping a nominal amount of Dy (1 at%) in HfO_2. **Figure 3.17 (b)**depicts two dimensional (x,y) CIE color space chromaticity diagram for HfO_2 nanoparticles doped with varying Dy concentration under an excitation of 352 nm. The CIE chromaticity coordinates are found to be (0.17, 0.12), (0.27, 0.27), (0.29, 0.29), (0.25, 0.24), (0.19, 0.13) and (0.19, 0.15) for x = 0, 0.01, 0.05, 0.07, 0.09 and 0.11, respectively. Among all samples, the color coordinates of x = 0.01, 0.05 and 0.07 are close to that of the cool white emission having the highest Y-B ratio. This indicates that by adjusting the Y-B ratio, one can also realize white light emission in Dy doped HfO_2 system for white LED (WLED) and display application.

3.2.9 Energy Band Diagram

We have proposed an energy band diagram to illustrate the different energetic transitions involved in Dy doped HfO_2 system as shown in **figure 3.18**. We have labeled

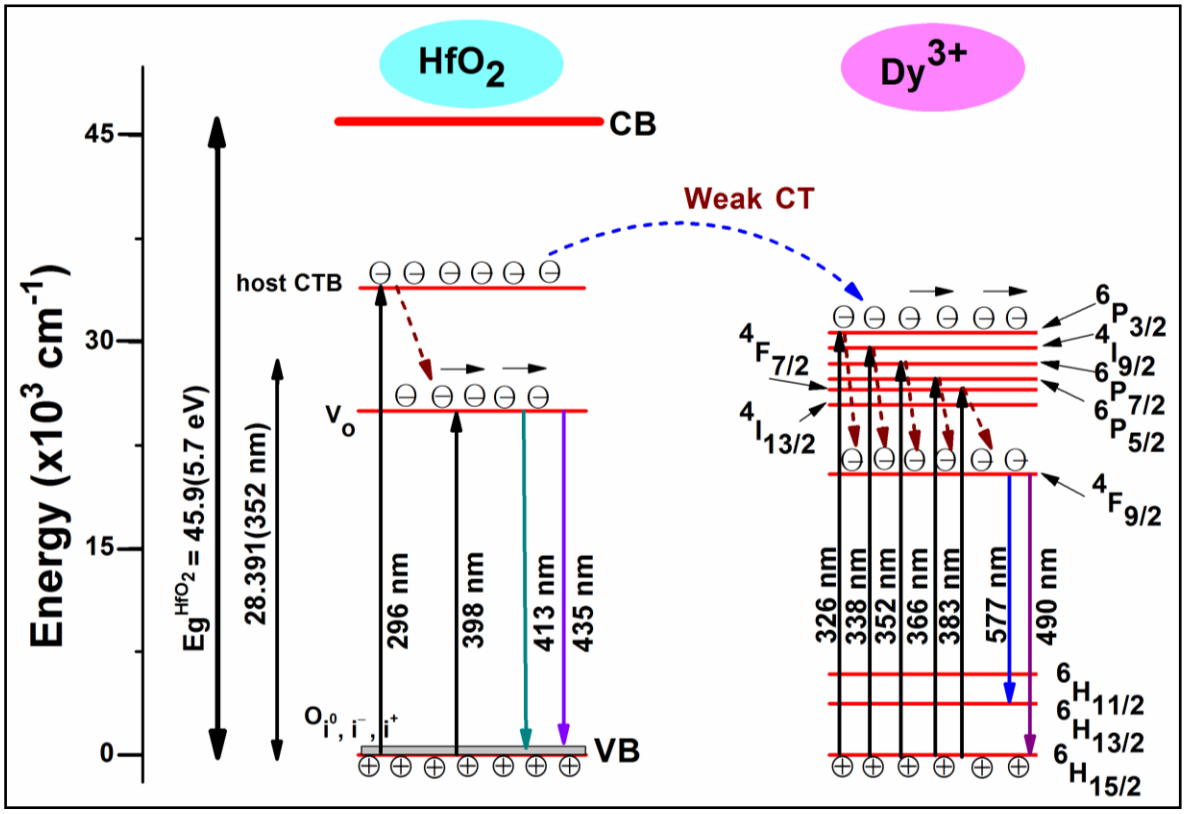

Figure 3.18 *The proposed energy band diagram illustrating the charge transfer (CT) mechanism taking place in* $Hf_{1-x}Dy_xO_2$.

the energy levels associated with the excitation and emission of Dy^{3+} ions ($^6H_{11/2}$, $^6H_{13/2}$, $^6H_{15/2}$, $^4F_{9/2}$, $^4I_{13/2}$, $^4F_{7/2}$, $^6P_{5/2}$, $^6P_{7/2}$, $^6P_{3/2}$ and $^4I_{9/2}$) and the host lattice (V_o, O_i^o, O_i^- and O_i^+). The host HfO_2 (donor) partially absorbs the pumping energy and the electrons are promoted either to the host charge transfer band (CTB) and/or to the inherent defect states (V_o) lying within the band gap of the host observed at ~296 and 398 nm in the excitation spectrum.

Consequently, the excited electrons relax from energy levels of the host CTB and from V_o defect states to the ground state through deep defect levels lying near to the valence band of the host showing emissions at ~413 and 435 nm and/or is partially transferred from the host CTB to different energy levels of the Dy^{3+} ion. The slight overlapping of HfO_2 broadband emission with Dy doped HfO_2 excitation band confirms the weak charge transfer from the host CTB to Dy^{3+} activator (acceptor) ions. The similar emission profiles of the host suggest that the energy transfer process could be non-radiative.[139] Such charge transfers from the host CTB to an activator ion (Sm^{3+} ions) have been shown by De la Rosa-Cruz *et al*. in Sm doped ZrO_2.[140] The electrons in the excited levels of Dy^{3+} ion relax to different ground states such as $^6H_{13/2}$ and $^6H_{15/2}$ through metastable state, $^4F_{9/2}$ showing emissions at 490 and 577 nm.

3.3 Conclusions

In this chapter, HfO_2 and Dy doped HfO_2 synthesized through simple Pechini type sol-gel method were thoroughly studied for structure, magnetic and photoluminescence properties. We demonstrated that the monoclinic phase of HfO_2 nanoparticles transforms partially to cubic phase after incorporating Dy of 5 at%. Further increasing Dy (x = 0.07-0.11) concentration, the cubic phase enhanced at the expense of monoclinic one. At x = 0.11, the monoclinic phase completely transformed to cubic phase. We could able to stabilize the high temperature cubic phase of HfO_2 at room temperature after incorporating Dy. Selected area electron diffraction patterns confirmed the monoclinic and cubic phase in HfO_2 and $Hf_{0.89}Dy_{0.11}O_2$, respectively. High resolution TEM showed interplanar spacing of ~0.28 and ~0.308 nm corresponding to (200) and (111) of $P2_1/c$ and $Fm\bar{3}m$, respectively. A mechanism for stabilization of high temperature cubic phase in $Hf_{1-x}Dy_xO_2$ was proposed

where role of the substitution effect of Dy and the formation of oxygen vacancies was discussed. The magnetic properties of HfO_2 nanoparticles revealed the presence of hysteresis at room temperature indicating ferromagnetism in contrast to the diamagnetic behavior in bulk. Incorporation of even 1 at% of Dy quenched the ferromagnetic ordering. The disappearance of ferromagnetic behavior in Dy doped HfO_2 could be due to the formation of defect complex Dy^{3+}─V_0─Dy^{3+} which mainly creates F^{++} centers, highly unfavorable for long range ferromagnetic ordering. From the photoluminescence studies, we observed an excellent blue and yellow light emission by incorporating even 1 at% of Dy in HfO_2 lattice. The peak intensity of the blue and yellow emission decreased with increasing Dy concentration. The emissions of Dy^{3+} ion were found to be partially accompanied by a non-radiative weak energy transfer from the host CTB to Dy^{3+} activator ions. Combining all the photoluminescence properties, we proposed an energy band diagram showing different transitions occurring in $Hf_{1-x}Dy_xO_2$. Looking at the rich photoluminescence behavior of $Hf_{0.99}Dy_{0.01}O_2$, it may be used as an efficient phosphor material for scintillator application.